

Electron-Cloud Build-Up Simulations for the FNAL Main Injector*

M. A. Furman,[†] Center for Beam Physics, LBNL, Berkeley, CA 94720-8211, USA

Abstract

We present a summary on ongoing simulation results for the electron-cloud (EC) buildup in the context of the proposed FNAL Main Injector (MI) intensity upgrade effort [1]. Most of the results presented here are for the field-free region at the location of the retarding field analyzer (RFA) electron detector [2–4]. The primary input variable we exercise is the peak secondary electron yield (SEY) δ_{\max} , which we let vary in the range $1.2 \leq \delta_{\max} \leq 1.7$. By combining our simulated results for the electron flux at the vacuum chamber wall with the corresponding RFA measurements we infer that $1.25 \lesssim \delta_{\max} \lesssim 1.35$ at this location. From this piece of information we estimate features of the EC distribution for various fill patterns, including the average electron number density n_e . We then compare the behavior of the EC for a hypothetical RF frequency $f_{\text{RF}} = 212$ MHz with the current 53 MHz for a given total beam population N_{tot} . The density n_e goes through a clear threshold as a function of N_{tot} in a field-free region. As expected, the higher frequency leads to a weaker EC effect: the threshold in N_{tot} is a factor ~ 2 higher for $f_{\text{RF}} = 212$ MHz than for 53 MHz, and n_e is correspondingly lower by a factor ~ 2 when N_{tot} is above threshold. We briefly describe further work that needs to be carried out, sensitivities in the calculation, and puzzles in the results that remain to be addressed.

INTRODUCTION

An upgrade to the MI at FNAL is being considered that would increase the bunch intensity N_b from the present $\sim 6 \times 10^{10}$ to $\sim 30 \times 10^{10}$ in order to generate intense beams for the neutrino program [1]. Such an increase in beam intensity would place the MI in a parameter regime where other storage rings have seen a significant EC effect. Motivated by this concern, efforts have been undertaken over the recent past to measure [2–4] and simulate [5–12] the magnitude of the effect and to assess its operational implications on the proposed upgrade.

Although achieving such high intensities will require significant hardware upgrades, the technique of slip-stacking the bunch trains generated by the booster allows, at present, bunch intensities $N_b \gtrsim 10 \times 10^{10}$ in the MI, though not for all fill patterns achievable at lower intensities. During 2006 an RFA-type electron detector was installed in a field-free straight section of the MI which has been used to measure the EC flux at the walls of the vacuum

chamber [2–4]. The one-turn-averaged, volume-averaged, EC number density n_e inferred from these measurements is sufficiently low that it is not expected to cause significant detrimental effects on the beam. This absence of an effect is, indeed, consistent with observations. Nevertheless, the RFA signal obtained at the highest achieved beam intensities is sufficiently clear to allow a first calibration of the simulation codes and therefore a sharpening of their predictions, and to better evaluate options for the proposed intensity upgrade.

In this article we present the current status of the EC build-up simulations by means of the build-up code POSINST [13–16], and their calibration against the above-mentioned RFA measurements. By comparing our simulations against measurements, and subject to reasonable assumptions, we conclude that δ_{\max} was in the range $1.25 \lesssim \delta_{\max} \lesssim 1.35$ at the location of the RFA when the measurements were taken [3].¹ We compare the EC build-up in the RFA field-free region with the build-up in a dipole bending magnet. We find a qualitative difference between the two: n_e shows a clear threshold behavior as a function of δ_{\max} in the field-free region but not in the dipole magnet. In this latter case, n_e is higher by a factor of ~ 3 than in the field-free region at the same beam intensity provided threshold is exceeded in the field-free region. We then compare the EC build-up for a hypothetical RF frequency $f_{\text{RF}} = 212$ MHz with the current value of 53 MHz, for a given total beam population N_{tot} . We carry out the comparison of the two frequencies in the range $3.29 \times 10^{13} \leq N_{\text{tot}} \leq 16.4 \times 10^{13}$, which roughly corresponds to the range $6 \times 10^{10} < N_b < 30 \times 10^{10}$ in bunch intensity. In the field-free region we see a strong threshold behavior of n_e as a function of N_{tot} at fixed δ_{\max} , consistent with earlier simulations [5–11]. For $f_{\text{RF}} = 212$ MHz, the threshold value of N_{tot} is higher by a factor ~ 2 than for 53 MHz, and the value of n_e is correspondingly lower by a factor of ~ 2 . Initial results of this comparison were described in Ref. 12. The corresponding comparison of the EC build-up for the two RF frequencies in a dipole bending magnet remains to be carried out, and certain puzzles in our results remain to be explained.

FIELD-FREE REGION

Summary of Measurements

We are concerned here only with measurements taken for eight specific fill patterns. In these measurements a beam of 3, 4 or 5 booster trains was used, each train consisting of 81 consecutive filled buckets of bunch intensity

*Work supported by the FNAL MI upgrade R&D effort and by the US DOE under contract DE-AC02-05CH11231. Invited talk, Proc. HB2008, Nashville, August 25-29, 2008. <http://neutrons.ornl.gov/workshops/hb2008/>.

[†]mafurman@lbl.gov

¹In general, δ_{\max} can increase due to venting of the chamber to air, or decrease due to beam-induced conditioning.

Table 1: Fill patterns analyzed.

Case	No. trains	N_b [10^{10}]	Comment
1a	5	9.7	even gaps
1b	5	9.0	even gaps
1c	5	8.1	even gaps
1d	5	7.2	even gaps
2a	4	9.5	even gaps
2b	4	9.1	even gaps
3	4	9.5	uneven gaps
4	3	9.1	even gaps

N_b as indicated in Tab. 1. For cases 1, 2 and 4, the trains were equally spaced, with a gap of 5 empty buckets between trains, in addition to a long abort gap of 77 empty buckets (the harmonic number is $h = 588$). For case 3, one of the trains was spaced further away from the other three, by a gap of 42 empty buckets. The MI beam ramps from injection at $E_b = 8.9$ GeV to extraction at 120 GeV in ~ 0.5 s, corresponding to $\sim 45,000$ revolutions. The beam crosses transition at $E_b \gtrsim 20$ GeV. The RFA is installed at the top of a free-field round chamber. It presents to the beam a circular opening 1" in diameter. The RFA signal was recorded during the full energy ramp. Using the known acceptance of the RFA and its $V-A$ calibration, the incident electron flux J_e was inferred from the RFA signal, as shown in Fig. 1. For reasons that are not well understood, the RFA signal peaks in all cases at $E_b \simeq 60$ GeV, and it is for this beam energy that the value of J_e is plotted in Fig. 1. We will address this issue in the discussion below.

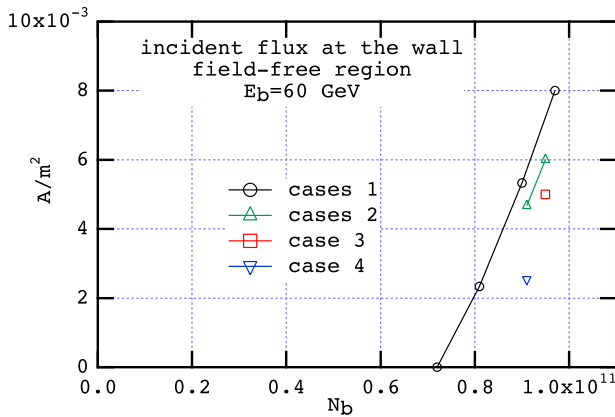


Figure 1: Electron flux incident on the vacuum chamber wall inferred from the RFA measurements in a field-free region, at $E_b = 60$ GeV. Each point on this plot represents a “case,” as listed on Table. 1.

Simulation Conditions

Ideally we would simulate the entire energy ramp, but this is wholly beyond our present-day computer capabilities. We have therefore simulated the EC build-up only for one full MI revolution for each case (the revolution period, $T_0 = 11.1 \mu\text{s}$, is much longer than necessary for the EC to reach a steady state, hence the one-turn averages sensibly represent steady-state values), and only for a few selected values of E_b during the ramp. For each value of E_b we used the actually measured value of the RMS bunch length σ_z , as shown in Fig. 2, and the corresponding transverse RMS beam sizes σ_x and σ_y at the RFA location. For the purposes of comparing our simulations against measurements, however, we select only $E_b = 60$ GeV. CPU running time on a Macintosh G5 (1.8 GHz) is 1.5–2.5 hrs for one MI revolution, depending on which parameter set is chosen. Relevant machine and simulation parameters are listed in Tab. 2.

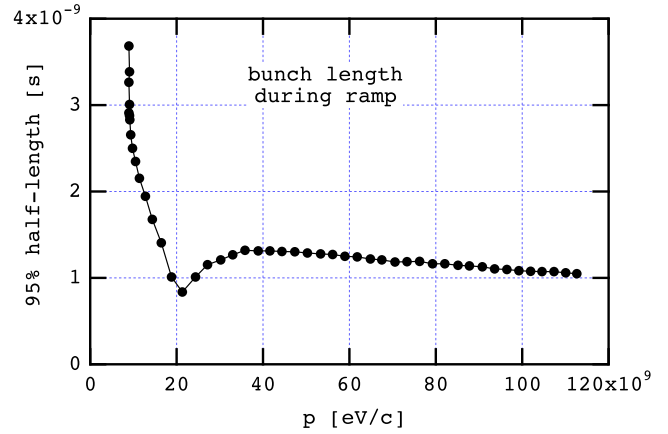


Figure 2: Bunch length vs. beam momentum during the MI ramp. Transition is crossed just above 20 GeV/c.

Concerning the source of electrons, we assume here that the main primary-electron source mechanism is ionization of residual gas, with pressure and temperature as listed in Tab. 2. We choose an artificially high pressure of 20 nTorr for the purposes of speeding up the simulated EC build-up; since the EC is dominated by secondary electron emission off the walls of the chamber, the details of the primary mechanism are not very important. We assume that the SEY model described in [14, 15] is applicable to the MI stainless steel vacuum chamber, with the additional practical assumption that the SEY at 0 energy, $\delta(0)$, is proportional to δ_{max} , $\delta(0)/\delta_{\text{max}} = 0.2438$. The peak SEY δ_{max} is the primary variable exercised in this set of simulations: we allow it to take values through the range $1.2 \leq \delta_{\text{max}} \leq 1.7$. We keep E_{max} , the incident electron energy at which the SEY peaks, fixed at 293 eV.

Simulation results for the RFA

Two samples of the EC distribution, averaged in time over one full turn, are shown in Fig. 3. Results for J_e are

Table 2: Assumed MI parameters for EC simulations.

Ring and beam	
Ring circumference	$C = 3319.419 \text{ m}$
Revolution period	$T_0 = 11.13 \text{ } \mu\text{s}$
RF frequency	$f_{\text{RF}} = 52.809 \text{ MHz}$
Harmonic number	$h = 588$
Beam energy	$E_b = 60 \text{ GeV}$
Bunch profile	3D gaussian
Tr. RMS bunch sizes	$(\sigma_x, \sigma_y) = (0.866, 1.06) \text{ mm}$
RMS bunch length	$\sigma_z = 0.19 \text{ m}$
Pipe cross sect. at RFA	round
Pipe radius at RFA	$a = 7.3 \text{ cm}$
Pipe cross sect. at dipole	elliptical
Pipe semiaxes at dipole	$(a, b) = (6.15, 2.45) \text{ cm}$
Dipole field at $E_b = 60 \text{ GeV}$	$B = 0.69 \text{ T}$
Primary e^- sources	
Resid. gas pressure	$P = 20 \text{ nTorr}$
Temperature	$T = 305 \text{ K}$
Ioniz. cross-section	$\sigma_i = 2 \text{ Mbarns}$
Ioniz. e^- creation rate	$1.266 \times 10^{-7} \text{ (e/p)/m}$
Secondary e^- parameters	
Peak SEY	$\delta_{\text{max}} = 1.2 - 1.7$
Energy at δ_{max}	$E_{\text{max}} = 292.6 \text{ eV}$
SEY at 0 energy	$\delta(0) = 0.2438 \times \delta_{\text{max}}$
Simulation parameters	
Full bunch length	$L_b = 5\sigma_z$
Primary macroelectrons/bunch	100
Max. no. of macroelectrons	20000
No. kicks in L_b	$N_k = 253$
Integration time step	$4.8 \times 10^{-11} \text{ s}$
Space-charge grid	64×64

shown in Figs. 4 and 5. In this latter plot we also show the measured data for the eight cases (Fig. 1) superposed on the simulations. The intersections of the measurements with simulations show a set of solutions for δ_{max} in the range $1.25 \lesssim \delta_{\text{max}} \lesssim 1.35$. The fact that these solutions are reasonably well clustered suggests consistency of the model and of the measurements. The simulated values shown for J_e were obtained by averaging the incident flux during one full MI revolution over the entire chamber surface being simulated. Although the RFA only counts the electrons striking the top of the chamber within a 1''-diameter disk about the horizontal center, we prefer to plot the value of J_e averaged over the entire chamber surface. We have verified that this whole-surface average is virtually identical to the local average within the RFA disk owing to the approximately cylindrical nature of the problem. The whole-surface average has the advantage, of course, of being much less sensitive to statistical noise.

The corresponding one-turn averaged values of n_e are shown in Fig. 6. It is clear that J_e and n_e go through a threshold in δ_{max} : below (above) threshold, n_e has an

exponential (linear) dependence on δ_{max} . These behaviors are expected on general grounds: below threshold, the multiplicative effect of secondary emission leads to exponential growth. Above threshold a high enough value of n_e is reached that space-charge forces suppress any further growth. In the range $1.25 \lesssim \delta_{\text{max}} \lesssim 1.35$ the average density n_e is in the range $n_e \sim 10^{10} - 10^{11} \text{ m}^{-3}$ which is typically lower by an order of magnitude than the average beam neutralization level given by

$$n_b = \frac{N_b}{\pi a^2 \langle s_b \rangle} = \frac{N_{\text{tot}}}{\pi a^2 C} \quad (1)$$

where $\langle s_b \rangle = C/M$ is the average bunch spacing and M is the number of bunches stored in the ring. For this reason no significant effect on the beam is expected; indeed, this lack of an effect is consistent with observations.

Simulation Results for the Dipole Magnet

We have carried out EC build-up simulations in a dipole bending magnet at $E_b = 60 \text{ GeV}$. All simulation parameters are the same as for the RFA location, except that the chamber is elliptical with semi-axes $(a, b) = (6.15, 2.45) \text{ cm}$. The dipole field strength is 0.0115 T/(GeV/c) , ie. $B = 0.69 \text{ T}$ at 60 GeV/c . Other parameters are listed in Tab. 2.

The $x - y$ distribution of the time-averaged EC density is shown in Fig. 7, which should be compared with 3. The magnetic field effectively confines the electrons to tight vertical spirals, leading to the characteristic stripe structure seen in Fig. 7.

The averaged J_e and n_e are shown in Fig. 8, which should be compared with Figs. 4 and 6. It seems clear that, in this case, there is no threshold behavior as a function of δ_{max} . It is possible that the threshold occurs at lower values of δ_{max} than 1.2. It is also possible that the effectively one-dimensional nature of the build-up physics in the dipole, as compared to the two-dimensional nature in the field-free region, accounts for the qualitative difference between the two.

$f_{\text{RF}} = 53 \text{ MHz VS. } 212 \text{ MHz}$

One way to make the EC less intense is to spread out the beam charge along the circumference because less intense bunches naturally lead to lower-energy electrons hence, typically, to a lower effective SEY. To quantify the potential benefit of this effect for the MI, we have carried out a comparison of the current RF frequency, $f_{\text{RF}} = 53 \text{ MHz}$, with a hypothetical frequency 4 times higher,² for a given total beam population N_{tot} .

In this initial assessment, we have carried out a simplified simulation only at injection energy, $E_b = 8.9 \text{ GeV}$, and only in the field-free section at the location of the RFA. Furthermore, we assume a simplified fill pattern in which

²The precise values of f_{RF} are 52.809 and 211.24 MHz.

there is only one long train and one gap. Specifically, for each f_{RF} we assume a fill pattern as follows:

$$f_{\text{RF}} = \begin{cases} 53 \text{ MHz:} & 548 \text{ full} + 40 \text{ empty buckets} \\ 212 \text{ MHz:} & 2192 \text{ full} + 160 \text{ empty buckets} \end{cases} \quad (2)$$

For any given fill pattern all the bunches are assumed to have the same particle population N_b . When carrying out comparisons of the two RF frequencies, we assume that N_b for $f_{\text{RF}} = 212 \text{ MHz}$ is $1/4$ of the value for $f_{\text{RF}} = 53 \text{ MHz}$, so that N_{tot} is the same in both cases. The range of values explored for $f_{\text{RF}} = 53 \text{ MHz}$ is $N_b = (6 - 30) \times 10^{10}$, corresponding to $N_b = (1.5 - 7.5) \times 10^{10}$ for $f_{\text{RF}} = 212 \text{ MHz}$, and to $N_{\text{tot}} = (3.29 - 16.4) \times 10^{13}$ for either case. Concerning the RMS bunch length σ_z , we assume $\sigma_z = 0.75 \text{ m}$ for $f_{\text{RF}} = 53 \text{ MHz}$, and $\sigma_z = 0.75/4 = 0.1875 \text{ m}$ for $f_{\text{RF}} = 212 \text{ MHz}$. We assume the same SEY model as above, but we restrict δ_{max} to the range 1.2–1.4. Parameters specific to this exercise are listed in Tab. 3 [12]. Parameters that do not appear here are the same as in Tab. 2.

Results

Fig. 9 shows the average incident electron flux J_e at the walls of the chamber, which might be compared with the data in Fig. 4. The result that J_e is much lower for $E_b = 8.9 \text{ GeV}$ than at higher values of E_b is consistent with previous MI simulations in a somewhat similar parameter regime [8].

Figure 10 shows n_e vs. N_{tot} , along with the average beam neutralization density, Eq. 1. For sufficiently high δ_{max} and/or N_{tot} , the average EC density exceeds the beam neutralization level. This condition is typically a rough indication of the onset of significant effects on the beam such as single-bunch instability or emittance growth.

Figures 9 and 10 exhibit a clear threshold behavior in N_{tot} . Simple fits to these data show that when N_{tot} exceeds a certain value N_{th} , the average EC density grows like

$$n_e \simeq n_0(N_{\text{tot}} - N_{\text{th}}) \quad (3)$$

where $n_0 \simeq 0.04 \text{ m}^{-3}$, roughly independently of δ_{max} and f_{RF} . On the other hand, as shown in Fig. 11, the threshold N_{th} does depend on both δ_{max} and f_{RF} , in the form

$$N_{\text{th}} \simeq -N_0(\delta_{\text{max}} - \delta_0) \quad (4)$$

where $N_0 \simeq 2.5 \times 10^{14}$, roughly independently of f_{RF} , and

$$\delta_0 \simeq \begin{cases} 1.75, & f_{\text{RF}} = 53 \text{ MHz} \\ 1.55, & f_{\text{RF}} = 212 \text{ MHz} \end{cases} \quad (5)$$

The growth of n_e and J_e as a function of N_{tot} can be partially explained by the monotonic dependence of the electron-wall impact energy E_0 on N_{tot} , as shown in Fig. 12. As E_0 increases towards $E_{\text{max}} \simeq 293 \text{ eV}$, where $\delta(E_0)$ is maximum, one naturally expects an increase in the effective SEY, hence a larger electron density. This argument, however, does not explain the above-mentioned

threshold behavior, which probably involves a competition of opposing effects such as secondary emission, space-charge forces, and the partial absorption of low-energy electrons striking the walls.

CONCLUSIONS

By fitting our EC build-up simulations to the RFA-measured electron-wall flux in an MI field-free region we conclude that the peak SEY was in the range $1.25 \lesssim \delta_{\text{max}} \lesssim 1.35$ at the time of the measurements. This range of values is consistent with others for well-conditioned stainless steel [17]. Since δ_{max} is almost certainly the essential parameter that will determine the EC build-up level in the MI upgrade, bracketing its value allows for better quantitative predictions for higher intensities. At present beam intensities, our simulations show that, for this range of δ_{max} , the EC density is low enough not to lead to detrimental effects on the beam, a conclusion consistent with observations.

In the field-free region analyzed, the steady-state EC wall flux J_e and steady-state average density n_e show a threshold behavior as a function of δ_{max} at fixed beam intensity. The threshold probably indicates a transition from a secondary-emission-dominated regime to a space-charge dominated regime. This threshold behavior is not seen in the simulations for a dipole bending magnet for the range of values of δ_{max} explored in this article, namely $1.2 \leq \delta_{\text{max}} \leq 1.7$; more work is needed to understand this absence of threshold behavior. One qualitative difference between field-free and dipole regions is that the EC dynamics in the former is effectively two-dimensional, while it is one-dimensional in the latter. This difference may hold the key to the explanation.

There is one puzzling qualitative difference between measurements and simulations that remains to be explained: the RFA signal shows a strong dependence on beam energy during the ramp, typically peaking at $E_b \sim 60 \text{ GeV}$, while spot-check simulations for the field-free region carried out at $E_b = 8.9, 20, 45, 60$ and 90 GeV show virtually no dependence on E_b (for each simulated case we used the appropriate values for all energy-dependent parameters, in particular the RMS beam sizes). We further recall that transition energy is $\sim 20 \text{ GeV}$, which is significantly below the energy at which the RFA signal peaks. We do not have an explanation for this discrepancy. It is possible that our simulations do not accurately represent certain details of the actual situation; for example, a significant beam closed orbit shift during the ramp might affect the RFA signal, but this shift would not be taken into account in the simulation because the closed orbit goes exactly through the geometrical center of the chamber. Interestingly, measurements at the SPS show a qualitatively similar behavior as the MI: the SPS RFA signal is strongly energy-dependent and peaks at an energy significantly higher than transition energy [18]. We are not aware of an explanation for the effect at the SPS, although a correlation has been noted between the RFA sig-

Table 3: Assumed MI fill pattern parameters for RF frequency comparisons.

Parameter	Symbol [unit]	Value	
Ring and beam			
RF frequency	f_{RF} [MHz]	52.809	211.24
Harmonic number	h	588	2352
No. of bunches	M	548	2192
Gap length	\cdots [buckets]	40	160
Bunch spacing	\cdots [buckets]	1	1
Bunch spacing	t_b [ns]	18.94	4.734
Bunch population	N_b [10^{10}]	6 – 30	1.5 – 7.5
Transverse RMS bunch sizes	(σ_x, σ_y) [mm]	(2.3,2.8)	
RMS bunch length	σ_z [m]	0.75	0.1875
Total beam population	N_{tot} [10^{13}]	3.29 – 16.4	
Beam energy	E_b [GeV]	8.9	
Simulation parameters			
No. kicks in L_b	N_k [\cdots]	253	65
Integration time step	\cdots [s]	4.8×10^{-11}	

nal and an empirical but simple combination of powers of the transverse and longitudinal beam sizes.

When we compare the simulated EC build-up in the RFA field-free region for two RF frequencies, namely the current 53 MHz with a hypothetical 212 MHz, for a given total beam population N_{tot} , we observe a clear threshold behavior as a function of N_{tot} : when N_{tot} exceeds a value N_{th} , n_e increases proportionally to $(N_{\text{tot}} - N_{\text{th}})$; for $N_{\text{tot}} < N_{\text{th}}$, n_e grows exponentially with N_{tot} .

The threshold N_{th} has a sensitive inverse dependence on δ_{max} , and a sensitive direct dependence on f_{RF} : for a given δ_{max} , N_{th} is roughly a factor of 2 higher for $f_{\text{RF}} = 212$ MHz than for 53 MHz. For fixed N_{tot} , this qualitative beneficial effect of the higher f_{RF} can be expected on rather simple grounds, because the correspondingly lower value of N_b makes the electron-wall impacts less energetic hence less effective in generating secondary electrons.

The dependence of N_{th} on f_{RF} affords the possibility of dramatically reducing the EC density assuming one has some freedom to choose the value of N_{tot} . This is because there is always a range of N_{tot} for which the electron cloud is below threshold for $f_{\text{RF}} = 212$ MHz but above threshold for $f_{\text{RF}} = 53$ MHz. For example, in Fig. 10 (bottom) for the case $\delta_{\text{max}} = 1.3$ and $N_{\text{tot}} = 0.8 \times 10^{14}$, the simulated n_e is almost 5 orders of magnitude smaller for $f_{\text{RF}} = 212$ MHz than for 53 MHz. On the other hand, if the desired value of N_{tot} is so high that it exceeds threshold for $f_{\text{RF}} = 212$ MHz (and, *a fortiori*, for 53 MHz), then the beneficial effect of the higher f_{RF} is in the range of a factor of ~ 2 rather than several orders of magnitude. This, unfortunately, is the situation for the planned MI upgrade.

Although the RF frequencies comparison carried out here is based on a simplified beam fill pattern, and only for $E_b = 8.9$ GeV, we expect the qualitative features of our results to remain valid for more realistic patterns, in-

volving several gaps in the bunch train, provided the values of N_{tot} are in the range considered here. It seems important to repeat this exercise in a dipole on account of the observed qualitative difference in the simulations between a field-free region and a dipole field region.

We believe the conclusions reached here to be qualitatively correct; however, our simulations may be sensitive to variables that may change quantitative details of the results. Such variables may include:

- The precise value of $\delta(0)$.
- The detailed composition of the secondary emission energy spectrum, particularly the fraction of redifused electrons.
- The precise value of E_{max} .
- Computational parameters, such as the space-charge grid size and integration time step.

Although the simulation parameter values used here have been shown in previous similar work to yield reasonably converged results, we intend to verify this in the present context. We also intend to extend the work presented here by further exploring the physical parameter regime.

ACKNOWLEDGMENTS

I am indebted to I. Kourbanis and R. Zwaska for experimental results, many discussions and guidance.

REFERENCES

- [1] Proton Driver Study. II. (Part 1, ch. 13), FERMILAB-TM-2169 (G. W. Foster, W. Chou and E. Malamud, eds.), May 2002.

- [2] R. Zwaska, "Electron Cloud Measurements at the Fermilab Main Injector," Proc. International Workshop on Electron-Cloud Effects "ECLLOUD07" (Daegu, S. Korea, April 9-12, 2007), KEK Proceedings 2007-10, Dec. 2007-A, p. 97. <http://chep.knu.ac.kr/ecloud07/>
- [3] I. Kourbanis, "e-Cloud MI Measurements", 26 Aug. 2007.
- [4] R. Zwaska, these proceedings.
- [5] M. A. Furman, "A preliminary assessment of the electron cloud effect for the FNAL main injector upgrade," LBNL-57634/CBP-Note-712/FERMILAB-PUB-05-258-AD, 23 June 2006. A condensed version of this article, of the same title, is published in New J. Phys. **8** (2006) 279. <http://stacks.iop.org/1367-2630/8/279>
- [6] M. A. Furman, "Studies of e-cloud build up for the FNAL main injector and for the LHC," LBNL-60512/CBP Note-736, June 15, 2006; Proc. 39th ICFA Advanced Beam Dynamics Workshop on High Intensity High Brightness Hadron Beams "HB2006" (Tsukuba, Japan, May 29-June 2nd, 2006), paper TUAX05. <http://hb2006.kek.jp/>
- [7] M. A. Furman, "HINS R&D Collaboration on Electron Cloud Effects: Midyear Progress Report," CBP-Technote-364/FERMILAB-TM-2369-AD, 22 Sept. 2006.
- [8] M. A. Furman, "HINS R&D Collaboration on Electron Cloud Effects: Build-Up Simulations at the Electron Detector Location in the MI," CBP Technote-367, Dec. 5, 2006.
- [9] M. A. Furman, K. Sonnad and J.-L. Vay, "HINS R&D Collaboration on Electron Cloud Effects: Midyear Report," LBNL-61921/CBP-761/FERMILAB-TM-2370-AD, Nov. 7, 2006.
- [10] M. A. Furman, "Electron-Cloud Build-up in the FNAL Main Injector," LBNL-62738, June 4, 2007. Proc. Intl. Wkshp. on Electron-Cloud Effects "ECLLOUD07" (Daegu, S. Korea, April 9-12, 2007), [http://chep.knu.ac.kr/electron cloud07/](http://chep.knu.ac.kr/electron%20cloud07/)
- [11] M. A. Furman, "Electron-Cloud Build-Up Simulations for the MI RFA: A Status Report," CBP-technote-387, 12 Nov. 2007, presented at the Project X Workshop, FNAL, 12-13 Nov., 2007. <http://projectx.fnal.gov/Workshop/Index.htm>
- [12] M. A. Furman, "Main Injector Upgrade R&D Collaboration on Electron Cloud Effects: Comparing the RF frequency of 53 MHz vs. 212 MHz," CBP-Technote-386, 17 March 2008.
- [13] M. A. Furman and G. R. Lambertson, "The electron-cloud instability in the arcs of the PEP-II positron ring," LBNL-41123/CBP Note-246, PEP-II AP Note AP 97.27 (Nov. 25, 1997). Proc. *Intl. Workshop on Multibunch Instabilities in Future Electron and Positron Accelerators "MBI-97"* (KEK, 15-18 July 1997; Y. H. Chin, ed.), KEK Proceedings **97-17**, Dec. 1997, p. 170.
- [14] M. A. Furman and M. T. F. Pivi, "Probabilistic model for the simulation of secondary electron emission," LBNL-49771/CBP Note-415 (Nov. 6, 2002). PRST-AB **5** 124404 (2003), <http://prst-ab.aps.org/pdf/PRSTAB/v5/i12/e124404>.
- [15] M. A. Furman and M. T. F. Pivi, "Simulation of secondary electron emission based on a phenomenological probabilistic model," LBNL-52807/SLAC-PUB-9912 (June 2, 2003).
- [16] M. A. Furman, "The electron-cloud effect in the arcs of the LHC," LBNL-41482/CBP Note 247/LHC Project Report 180 (May 20, 1998).
- [17] M. A. Furman, "Formation and Dissipation of the Electron Cloud," LBNL-51829; Proc. PAC03 (Portland, OR, May 12-16, 2003), paper TOPC001.
- [18] G. Arduini, T. Bohl, K. Cornelis, W. Höfle, E. Métral and F. Zimmermann, "Beam Observations with Electron Cloud in the CERN PS & SPS Complex," Proc. 31st ICFA Advanced Beam Dynamics Workshop on Electron-Cloud Effects "ECLLOUD04" (Napa, California, April 19-23, 2004; M. Furman, S. Henderson and F. Zimmermann, eds.), CERN Yellow Report CERN-2005-001/CARE-Conf-05-001-HHH/LBNL-56372/SNS-10400000-TR0024-R00 <http://icfa-ecloud04.web.cern.ch/icfa-ecloud04/>

DISCLAIMER

This document was prepared as an account of work sponsored by the United States Government. While this document is believed to contain correct information, neither the United States Government nor any agency thereof, nor The Regents of the University of California, nor any of their employees, makes any warranty, express or implied, or assumes any legal responsibility for the accuracy, completeness, or usefulness of any information, apparatus, product, or process disclosed, or represents that its use would not infringe privately owned rights. Reference herein to any specific commercial product, process, or service by its trade name, trademark, manufacturer, or otherwise, does not necessarily constitute or imply its endorsement, recommendation, or favoring by the United States Government or any agency thereof, or The Regents of the University of California. The views and opinions of authors expressed herein do not necessarily state or reflect those of the United States Government or any agency thereof, or The Regents of the University of California.

Ernest Orlando Lawrence Berkeley National Laboratory is an equal opportunity employer.

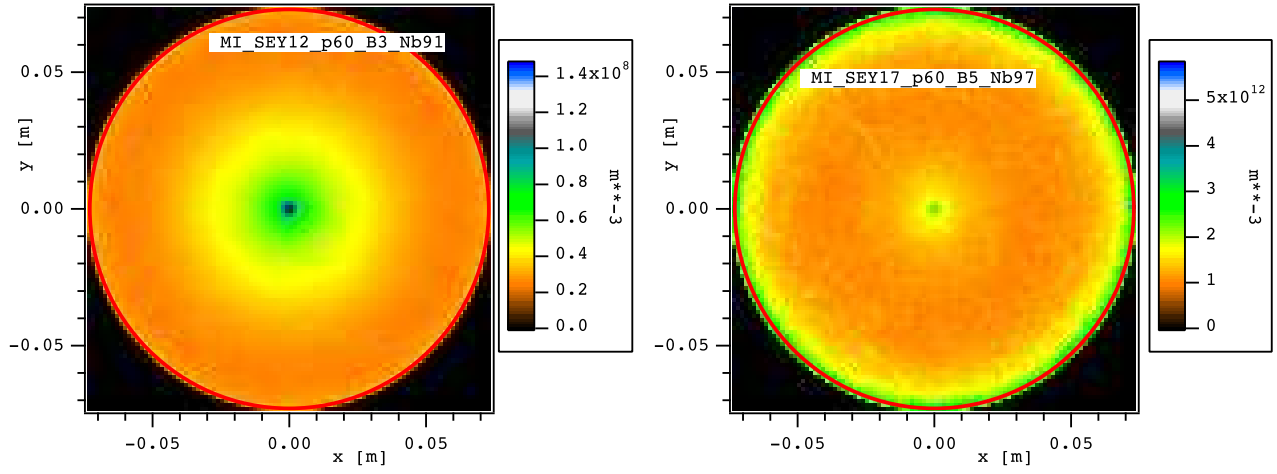


Figure 3: Simulated EC number density distribution in the field-free location. The distribution is averaged over time during one MI revolution for $E_b = 60$ GeV. The beam (not shown) travels perpendicularly to the page through the center of the chamber. The red circle represents the vacuum chamber boundary used in the simulation. Left: case 4, assuming $\delta_{\max} = 1.2$. Right: case 1a, assuming $\delta_{\max} = 1.7$.

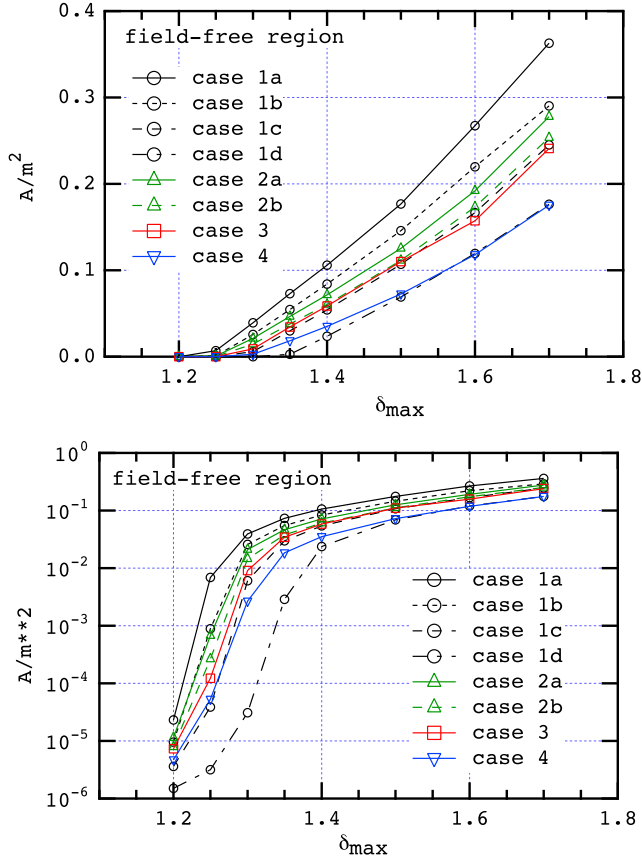


Figure 4: Simulated electron flux J_e incident on the vacuum chamber walls at the field-free region vs. the assumed value of δ_{\max} , at $E_b = 60$ GeV. The flux was averaged during one MI revolution and over the entire chamber surface. Top: linear scale; bottom: logarithmic scale (same data).

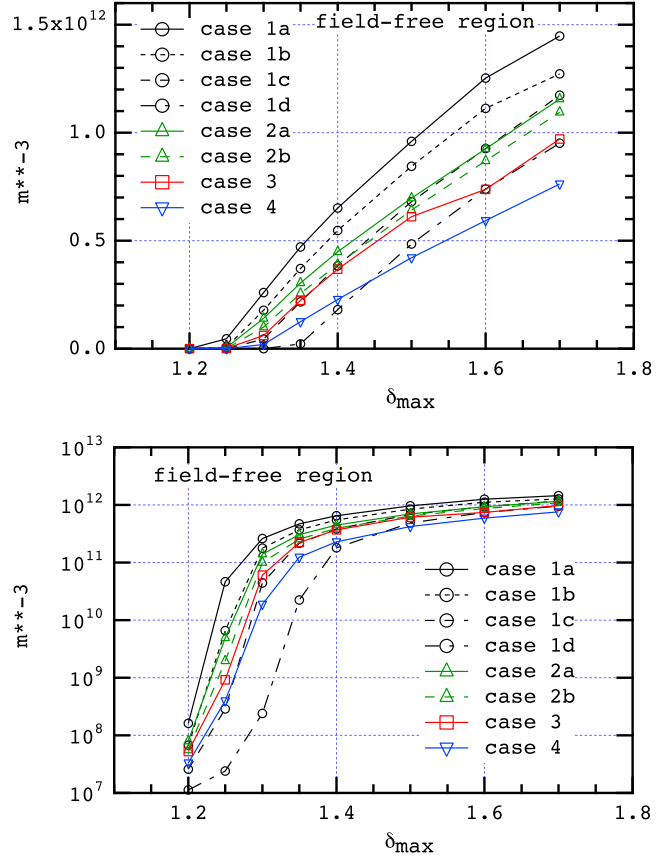


Figure 6: Simulated EC density at the field-free region where the RFA is installed vs. the assumed value of δ_{\max} , at $E_b = 60$ GeV. The density was averaged during one MI revolution and over the entire volume of the chamber section being simulated. Top and bottom are the same simulated data, plotted with linear and logarithmic scales respectively.

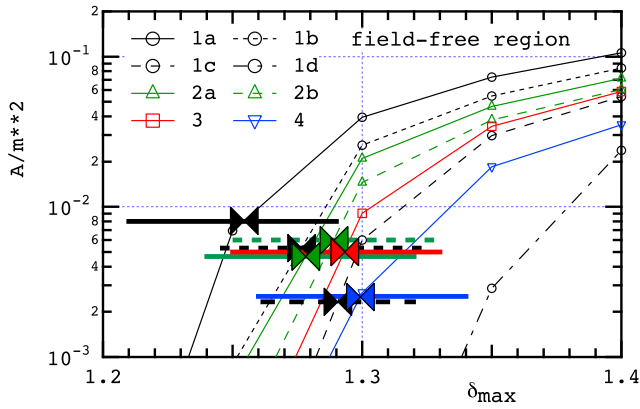


Figure 5: Detail of the simulated electron flux J_e (Fig. 4 bottom) plotted along with the RFA measurements, taken from Fig. 1, for each case (thick horizontal lines). The intersections of the measurements with the simulations, indicated by bowties, imply $1.25 \lesssim \delta_{\max} \lesssim 1.35$.

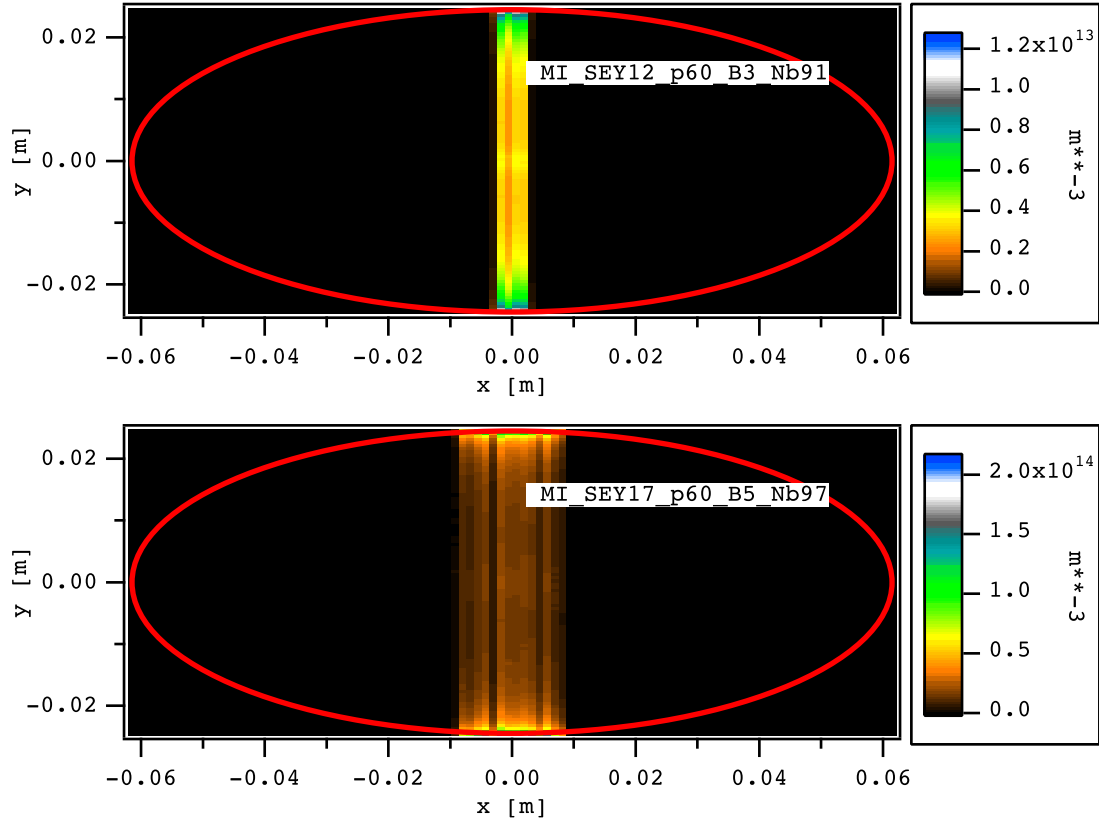


Figure 7: Simulated EC density distribution in a dipole bending magnet, averaged over time during one MI revolution for $E_b = 60$ GeV. The red ellipse represents the vacuum chamber boundary used in the simulation. Top: case 4, assuming $\delta_{\max} = 1.2$. Bottom: case 1a, assuming $\delta_{\max} = 1.7$. The slight left-right asymmetry of the density about $x = 0$ is due to numerical fluctuations and the binning algorithm; this asymmetry is expected to disappear with higher statistics.

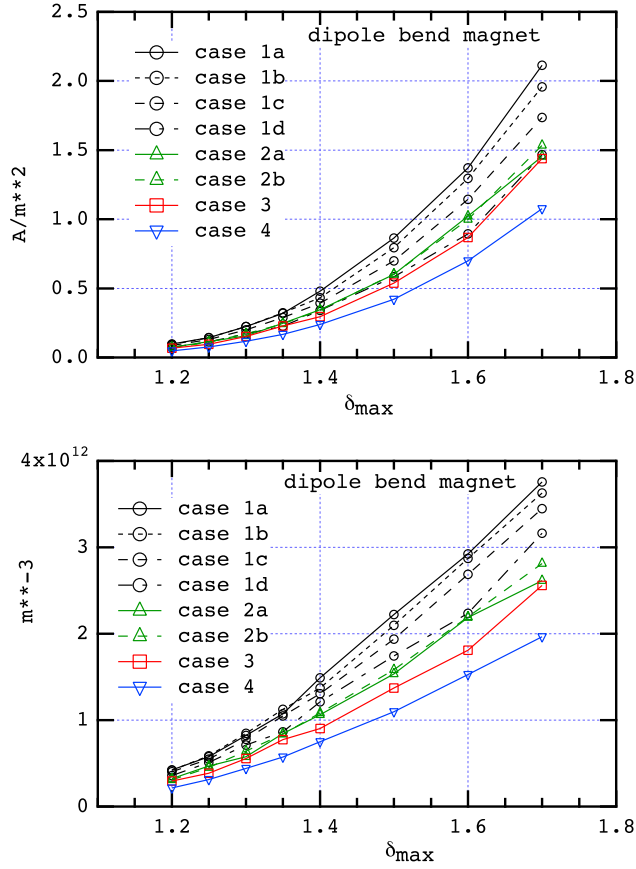


Figure 8: Simulated EC flux at the wall (top), and volumetric density (bottom) in a dipole bend vs. the assumed value of δ_{max} , at $E_b = 60$ GeV. The quantities were averaged during one MI revolution. The flux was averaged over the entire chamber surface, and the density over the entire volume.

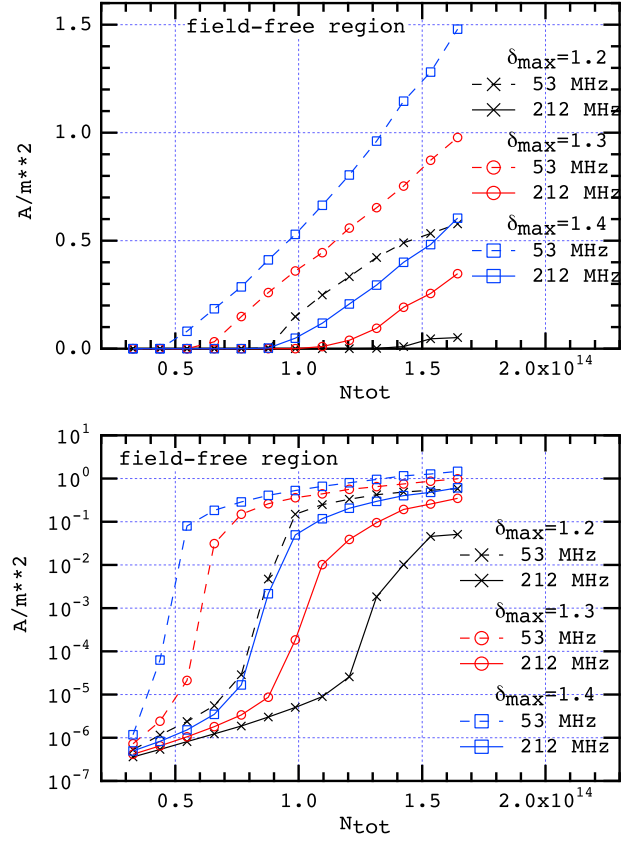


Figure 9: Average simulated J_e at the RFA location for $E_b = 8.9$ GeV and $\delta_{max} = 1.2, 1.3$ and 1.4 . Top: linear scale; bottom: log scale (same data).

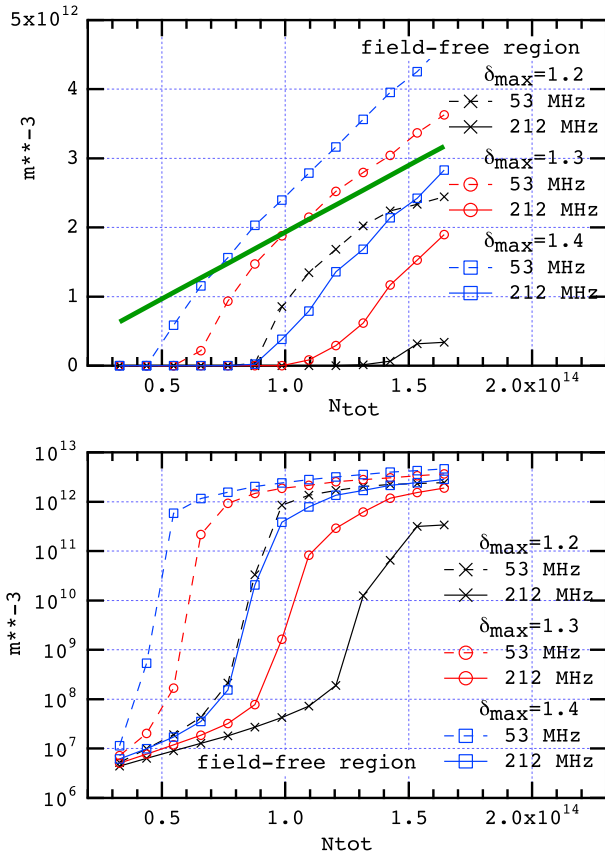


Figure 10: Average simulated n_e . Top: linear scale; bottom: log scale (same data). The straight green line in the top plot is the average beam neutralization density, Eq. (1).

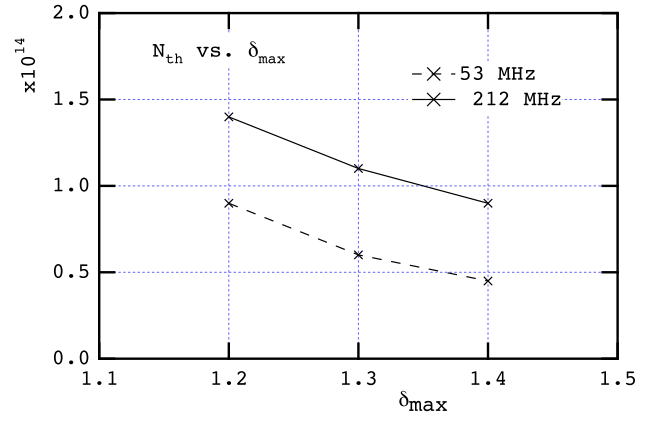


Figure 11: N_{th} vs. δ_{max} , Eqs. (4-5).

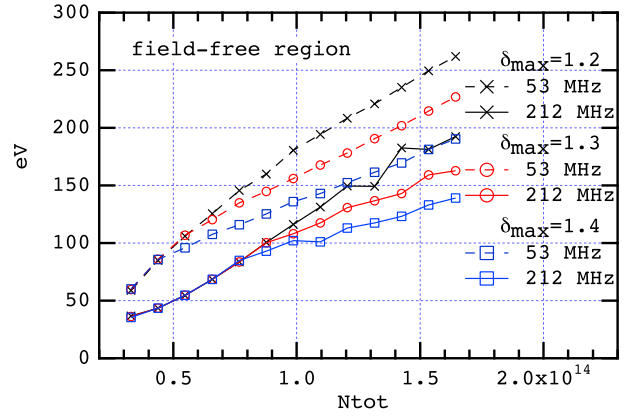


Figure 12: Average simulated electron-wall impact kinetic energy, per electron-wall collision.